

BeamVQ: Beam Search with Vector Quantization to Mitigate Data Scarcity in Physical Spatiotemporal Forecasting

Weiyan Wang¹ Xingjian Shi² Ruiqi Shu³ Yuan Gao³ Rui Ray Chen⁴ Kun Wang⁵ Fan Xu⁶ Jinbao Xue¹
Shuaipeng Li¹ Yangyu Tao¹ Di Wang¹ Hao Wu^{1,3,6} Xiaomeng Huang³

Abstract

In practice, physical spatiotemporal forecasting can suffer from data scarcity, because collecting large-scale data is non-trivial, especially for extreme events. Hence, we propose BeamVQ, a novel probabilistic framework to realize iterative self-training with new self-ensemble strategies, achieving better physical consistency and generalization on extreme events. Following any base forecasting model, we can encode its deterministic outputs into a latent space and retrieve multiple codebook entries to generate probabilistic outputs. Then BeamVQ extends the beam search from discrete spaces to the continuous state spaces in this field. We can further employ domain-specific metrics (e.g., Critical Success Index for extreme events) to filter out the top-k candidates and develop the new self-ensemble strategy by combining the high-quality candidates. The self-ensemble can not only improve the inference quality and robustness but also iteratively augment the training datasets during continuous self-training. Consequently, BeamVQ realizes the exploration of rare but critical phenomena beyond the original dataset. Comprehensive experiments on different benchmarks and backbones show that BeamVQ consistently reduces forecasting MSE (up to 39%), enhancing extreme events detection and proving its effectiveness in handling data scarcity. Our codes are available at <https://github.com/easylearningscores/BeamVQ>.

¹TEG, Tencent ²Boson AI ³Department of Earth System Science, Ministry of Education Key Laboratory for Earth System Modeling, Institute for Global Change Studies, Tsinghua University ⁴Institute for Interdisciplinary Information Sciences, Tsinghua University ⁵School of Computer Science and Engineering, Nanyang Technological University ⁶Department and Computer and Science, University of Science and Technology of China. Correspondence to: Xiaomeng Huang <hxm@tsinghua.edu.cn>.

Preliminary work. Under review. Do not distribute.

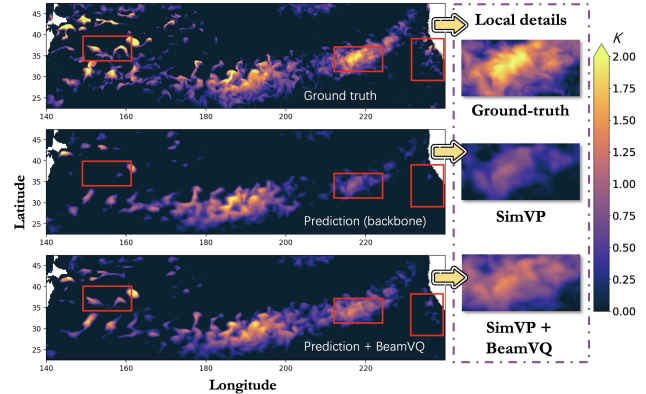


Figure 1: The visualization of extreme marine heatwave events shows that BeamVQ enhances Backbone models and improves their ability to capture extreme events. Detailed experimental results are provided in the experiments section.

1. Introduction

In physical spatiotemporal forecasting (e.g., meteorological forecasting (Bi et al., 2023; Lam et al., 2022), fluid simulation (Wu et al., 2024b; Wu et al.), and various multi-physics system models (Li et al., 2020; Wu et al., 2024c)), researchers typically need to capture physical patterns and predict extreme events, such as heavy rainfall due to severe convective weather (Ravuri et al., 2021; Doswell III, 2001), marine heatwave (Frölicher et al., 2018), and intense turbulence (Moisy & Jiménez, 2004)). However, they suffer from the fundamental problem of data scarcity to ensure physical consistency and accurately predict extreme events. Collecting large-scale and high-resolution physical data can be expensive and even infeasible. Consequently, limited training data can prevent data driven models (Sun et al., 2020; Zhu et al., 2019) like physics-informed neural networks (Raissi et al., 2019) from generalizing well, even though they have adopted physical laws as prior knowledge. Furthermore, extreme events occur infrequently in nature, making their labeled data quite sparse and imbalanced throughout the entire data set. Therefore, data-driven methods usually fail to capture these low-probability phenomena.

Existing studies on physical spatiotemporal forecasting belong to two categories, namely *Numerical Methods* and *Data-driven Methods*. Traditional numerical methods like finite difference and finite element simulate future changes by solving physical equations (Jouvet et al., 2009; Rogallo & Moin, 1984; Orszag & Israeli, 1974). Although these numerical methods can be consistent with fundamental physical principles, they not only suffer incredibly expensive computations but also can be infeasible, if we cannot fully understand the underlying mechanism of complex or rare physical events (Takamoto et al., 2022). Moreover, they are sensitive to the input disturbance (aka. the Butterfly Effect (Lorenz, 1972)), so they usually perturb initial conditions with different random noises to make multiple predictions for ensemble forecasting (Leutbecher & Palmer, 2008; Karlbauer et al., 2024), resulting in even higher time costs.

Driven by large-scale data, deep learning has emerged as the revolutionary approach for complex physical systems (Shi et al., 2015; Gao et al., 2022; Tan et al., 2022). Some methods attempt to combine physical knowledge with model training for better physical consistency and generalization (Long et al., 2018; Greydanus et al., 2019; Cranmer et al., 2020). For example, PhyDNet (Guen & Thome, 2020) and FNO (Li et al., 2020) add physics-inspired operators into the deep networks. Some works also introduce generative settings into extreme weather simulations, but they require numerical simulations to generate enough artificial data (Zhang et al., 2023; Ravuri et al., 2021). Some works like PINN (Raissi et al., 2019; Li et al., 2021; Hansen et al., 2023) leverage physical equations as additional loss regularization, which only works on specific problems with simplified equations and fixed boundary conditions. PreDiff (Gao et al., 2023) trains a latent diffusion model with guidance from a physics-informed energy function. Since these works manipulate physical prior as soft constraints to optimize the statistical metrics across the existing data, they rely on large-scale and high-quality data that is non-trivial to collect. Worse still, extreme events are always a small proportion of the full set, leading to poor prediction.

Some works in other files have explored various techniques to alleviate the data shortage, but they focus on the classification tasks and exploit domain characters. For example, Computer Vision (CV) develops data augmentation like Mixup (Zhang, 2017), which mixes different images and their labels to generate new samples. Natural Language Processing (NLP) conducts self-training to make use of extra unlabeled data with pseudo labels (Du et al., 2020). CV also widely adopts self-ensemble like EMA models (Wang & Wang, 2022) to improve the robustness. However, physical spatiotemporal forecasting cannot directly adopt these domain-specific methods designed for classification tasks. More details about all related works are in Appendix B.

To mitigate the problem of *data scarcity* in physical spatiotemporal forecasting, we propose Beam Search with Vector Quantization (**BeamVQ**) to improve physic consistency and generalization on extreme events. At its core, it extends the beam search from discrete states typically in NLP to continuous state spaces of this field, enabling the self-ensemble of top-quality outputs for iterative self-training. Specifically, BeamVQ as a plugin, we can follow previous works to train a base spatiotemporal predictor to generate deterministic outputs. And we construct a variational quantization framework with a vector code book to realize the vector quantization (VQ) mechanism, which discretizes the continuous output spaces of the base prediction. Therefore, we can conduct beam searches through the time steps in physical spatiotemporal forecasting, in a similar way to NLP sentence generation. Through the beam search, we can filter out top-k good-quality candidates with any metrics (even the non-differentiable ones that cannot be directly optimized), leading to better exploration of possible future evolution paths. Then BeamVQ develops a new self-ensemble strategy by combining all the top-k candidates. Besides improving the final predicting quality and robustness, the self-ensemble of top candidates can work as additional pseudo samples to iteratively augment the data set for continuous self-training, resulting in better physical consistency and generalization even on extreme events. For example, Figure 1 demonstrates our capability in extreme marine heatwave events, whose frequency ranges from one to three annual events (Oliver et al., 2018).

In summary, BeamVQ has the following main contributions:

Novel Methodology. We introduce the BeamVQ framework, which discretizes outputs via Vector Quantization. By combining Beam Search and self-ensemble strategies, it efficiently explores possible future evolution paths. This approach can significantly enhances the capture of extreme events and increases prediction diversity.

New Training Strategy. During the self-training phase, we incorporate "pseudo-labeled" samples from beam search into the training data and iteratively update the model. This process effectively compensates for the lack of real labels and indirectly optimizes any metrics for better physical consistency.

Consistent Improvement. We conduct systematic evaluations on multiple datasets, including meteorological, fluid, and PDE simulations, and on different backbone networks such as CNN, RNN, and Transformer. BeamVQ reduces the average MSE by 18.97% \sim 39.08%, showing consistent and significant improvements in accuracy, extreme event capture, and physical plausibility, demonstrating our effectiveness in mitigating data scarcity.

2. Method

Problem Definition. We investigate spatiotemporal prediction tasks spanning meteorological forecasting (Bi et al., 2023), computational fluid dynamics (Wu et al., 2024b), and PDE-based systems (Wu et al., 2024c). The observational data is structured as a 4D tensor $\mathbf{X} \in \mathbb{R}^{T \times C \times H \times W}$, where T denotes temporal steps, C represents physical variables (temperature, pressure, velocity fields), and (H, W) specify spatial resolution. Our objective is to learn a parametric mapping $f_\Theta : \mathbf{X}_t \mapsto \hat{\mathbf{Y}}_{t+1}$ that predicts subsequent system states from historical sequences $\mathbf{X}_t = \{\mathbf{X}_1, \dots, \mathbf{X}_t\}$. The parameters Θ are optimized through maximum likelihood estimation:

$$\Theta^* = \arg \max_{\Theta} \sum_{i=1}^T \log P(\mathbf{Y}_{t+1}^i | \mathbf{X}_t^i; \Theta) \quad (1)$$

where $P(\mathbf{Y}_{t+1}^i | \mathbf{X}_t^i; \Theta)$ defines the predictive distribution. The optimized model enables multi-step forecasting via iterative rollout $\hat{\mathbf{Y}}_{t+k} = f_\Theta(\{\mathbf{X}_t, \hat{\mathbf{Y}}_{t+1}, \dots, \hat{\mathbf{Y}}_{t+k-1}\})$, crucial for applications requiring temporal extrapolation in climate modeling (Bi et al., 2023), combustion dynamics (Anonymous, 2024), and fluid simulations (Wu et al.).

Architecture Overview. Our framework comprises three core stages of progressive refinement, as shown in Figure 2. Initially, we train a base spatiotemporal predictor f_Θ that processes historical observations $\mathbf{X}_t \in \mathbb{R}^{1 \times C \times H \times W}$ (single-step training) to generate next-step predictions $\hat{\mathbf{Y}}_{t+1} = f_\Theta(\mathbf{X}_t)$. Subsequently, we develop a Top-K VQ-VAE h_ϕ through codebook-based pretraining, where the encoder e_ϕ maps $\hat{\mathbf{Y}}_{t+1}$ to latent code \mathbf{z} , quantized via K-nearest codebook vectors $\{\mathbf{q}^{(k)}\}_{k=1}^K \subset \mathcal{C}$, followed by decoder d_ϕ reconstruction to yield diverse outputs $\{\tilde{\mathbf{Y}}_{t+1}^{(k)}\}$. During joint optimization, we employ a non-differentiable metric M (e.g., Critical Success Index (Gao et al., 2022)) to select the optimal reconstruction $\tilde{\mathbf{Y}}_{t+1}^*$, then minimize $\|\tilde{\mathbf{Y}}_{t+1}^* - \mathbf{Y}_{t+1}\|_2^2$ to refine f_Θ , while augmenting training data with ensemble averages of top- K' candidates. For multi-step inference, beam search (Steinbiss et al., 1994) maintains K trajectory candidates per step, progressively selecting optimal sequences through metric-guided pruning.

2.1. Stage 1: Pre-training the Base Prediction Model

We first develop a foundational predictor f_Θ that learns deterministic spatiotemporal dynamics from observational data. The model ingests input tensors $\mathbf{X}_t \in \mathbb{R}^{1 \times C \times H \times W}$ (single-step temporal context during training) and generates predictions $\hat{\mathbf{Y}}_{t+1} = f_\Theta(\mathbf{X}_t)$ through parametric mapping $f_\Theta : \mathbb{R}^{C \times H \times W} \rightarrow \mathbb{R}^{C \times H \times W}$. Architectural implementations are task-adaptive: Fourier Neural Operators (FNO) (Li et al., 2020) for spectral systems governed by PDEs, Vision Transformers (Dosovitskiy, 2020) for global dependency

modeling, or ConvLSTM (Shi et al., 2015) networks for local spatiotemporal correlations. The parameters Θ are learned by minimizing the reconstruction error:

$$\mathcal{L}_{\text{base}} = \mathbb{E} \left\| \hat{\mathbf{Y}}_{t+1} - \mathbf{Y}_{t+1} \right\|_2^2 \quad (2)$$

where the expectation is over training pairs $(\mathbf{X}_t, \mathbf{Y}_{t+1})$. Optimization employs gradient-based methods (Adam) (Kingma & Ba, 2014) with learning rate annealing, ensuring stable convergence. This stage establishes a strong deterministic prior that captures dominant physical patterns - for instance, FNO architectures learn Green's functions in Fourier space for fluid dynamics, while transformer variants attend to long-range atmospheric interactions. The trained f_{Θ^*} provides initial point estimates for subsequent uncertainty-aware refinement.

2.2. Stage 2: Top-K VQ-VAE Pre-training

We construct a variational quantization framework $h_\phi = (e_\phi, \mathcal{C}, d_\phi)$ to learn diverse reconstructions from deterministic predictions. Given the base model output $\hat{\mathbf{Y}}_{t+1}$, the encoder e_ϕ projects it to latent code:

$$\mathbf{z} = e_\phi(\hat{\mathbf{Y}}_{t+1}) \in \mathbb{R}^{d_z} \quad (3)$$

A codebook $\mathcal{C} = \{\mathbf{c}_i\}_{i=1}^N \subset \mathbb{R}^{d_z}$ with N entries enables Top-K vector quantization:

$$\mathbf{q}^{(k)} = \underset{\mathbf{c} \in \mathcal{C}}{\operatorname{argmin}} \|\mathbf{z} - \mathbf{c}\|_2^2 \quad \text{for } 1 \leq k \leq K \quad (4)$$

The decoder d_ϕ reconstructs K variants through parallel decoding:

$$\tilde{\mathbf{Y}}_{t+1}^{(k)} = d_\phi(\mathbf{q}^{(k)}), \quad 1 \leq k \leq K \quad (5)$$

The training objective combines three components:

$$\mathcal{L}_{\text{VQ}} = \underbrace{\|\tilde{\mathbf{Y}}_{t+1}^{(1)} - \mathbf{Y}_{t+1}\|_2^2}_{\text{Reconstruction}} + \underbrace{\|\operatorname{sg}[\mathbf{z}] - \mathbf{q}^{(1)}\|_2^2}_{\text{Codebook Learning}} + \beta \underbrace{\|\mathbf{z} - \operatorname{sg}[\mathbf{q}^{(1)}]\|_2^2}_{\text{Commitment}} \quad (6)$$

where $\operatorname{sg}[\cdot]$ denotes stop-gradient operator and β balances latent commitment. This design ensures: **(1)** Accurate primary mode reconstruction via $\tilde{\mathbf{Y}}_{t+1}^{(1)}$ optimization; **(2)** Codebook diversity preservation through Top-K retrieval; **(3)** Stable encoder-codebook alignment via commitment loss.

We conducted several experiments to verify the effect of selecting different K . And we use an optimization to explain how to choose K to achieve the best performance.

Theorem 1. *The best selection of K is determined by the numerical solution of the following optimization problem*

$$\arg \min_{\pi} h(\pi, \mathbb{T}) := \pi^\top A_{\mathbb{T}} \pi, \quad (7)$$

$$\text{subject to } \begin{cases} \sum_{i=1}^N \pi_i T_i \leq \alpha, \\ \sum_{i=1}^N \pi_i = 1, \\ 0 \leq \pi_i \leq m^{-1}, \quad 1 \leq i \leq N. \end{cases} \quad (8)$$

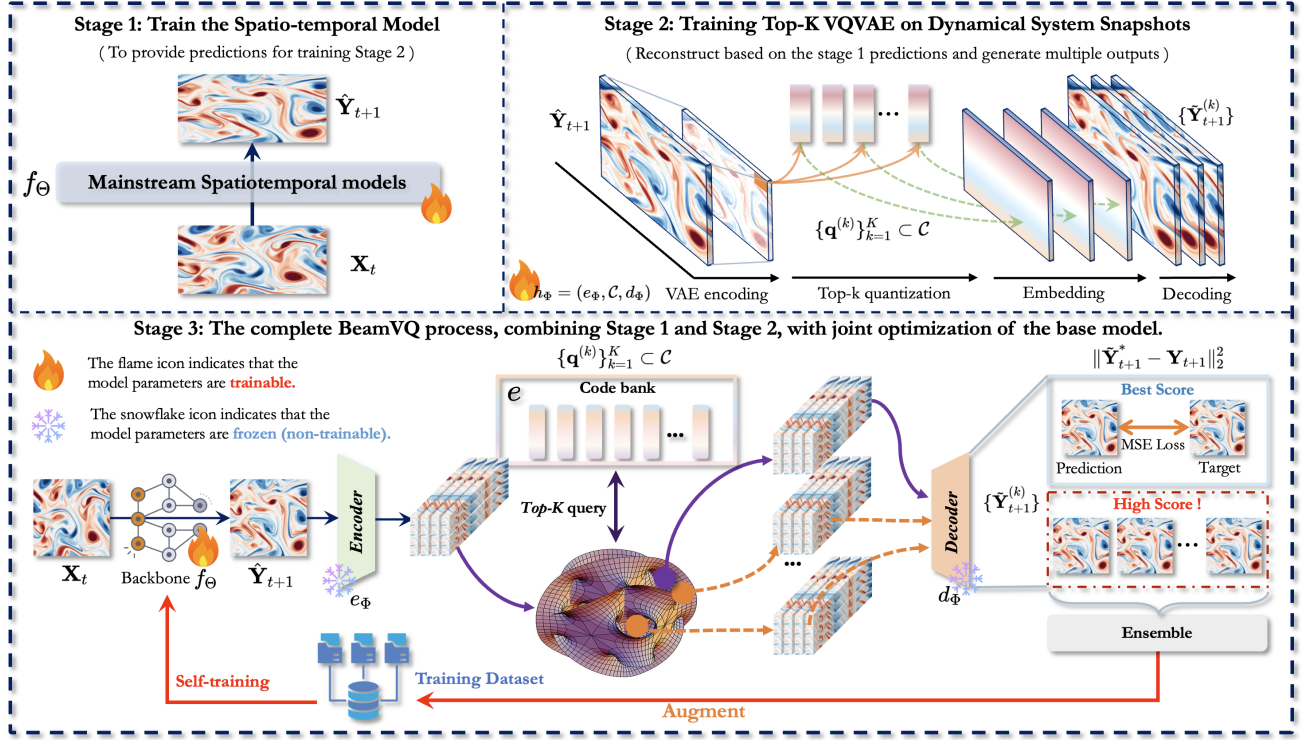


Figure 2: **Architecture Overview of BeamVQ.** (a) **Stage 1: Base Model Training:** A deterministic predictor (FNO/ViT/ConvLSTM) learns single-step mappings $\mathbf{X}_t \xrightarrow{f_{\Theta}} \hat{\mathbf{Y}}_{t+1}$ via MSE minimization. (b) **Stage 2: Top-K VQ-VAE:** Latent code \mathbf{z} from encoder e_{Φ} is quantized to K nearest codebook vectors $\{\mathbf{q}^{(k)}\}$, decoded to diverse predictions $\{\tilde{\mathbf{Y}}_{t+1}^{(k)}\}$. (c) **Joint Optimization:** The optimal reconstruction $\tilde{\mathbf{Y}}_{t+1}^*$ (selected by metric M) guides base model refinement, while top- K' ensemble $\tilde{\mathbf{Y}}_{t+1}$ enables self-training.

where π_i is the sampling probability of the augmented data

For details of the proof, please refer to Appendix C.

The pre-trained h_{Φ^*} establishes a structured latent manifold (Han et al., 2018) that encapsulates both predictive fidelity and uncertainty, which will be leveraged in Stage 3 for probabilistic refinement.

2.3. Stage 3: Joint Optimization

We develop a dual-phase optimization framework to refine the base predictor f_{Θ} using the frozen Top-K VQ-VAE h_{Φ} . The process iterates between:

$$\hat{\mathbf{Y}}_{t+1} = f_{\Theta}(\mathbf{X}_t), \quad \{\tilde{\mathbf{Y}}_{t+1}^{(k)}\}_{k=1}^K = h_{\Phi}(\hat{\mathbf{Y}}_{t+1}) \quad (9)$$

where h_{Φ} remains fixed with $\Phi = \Phi^*$ from Stage 2. A domain-specific metric M (e.g., Critical Success Index) evaluates each reconstruction:

$$s^{(k)} = M(\tilde{\mathbf{Y}}_{t+1}^{(k)}, \mathbf{Y}_{t+1}), \quad k \in [1, K] \quad (10)$$

Optimization Cycle is as follows:

1. **Optimal Guidance:** Select the highest-scoring variant

$$k^* = \arg \max_k s^{(k)}, \quad \mathcal{L}_{\text{guide}} = \|\tilde{\mathbf{Y}}_{t+1}^{(k^*)} - \mathbf{Y}_{t+1}\|_2^2 \quad (11)$$

2. **Ensemble Distillation:** Aggregate top- K' candidates

$$\tilde{\mathbf{Y}}_{t+1} = \frac{1}{K'} \sum_{k=1}^{K'} \tilde{\mathbf{Y}}_{t+1}^{(k_{\text{top}})} \quad (12)$$

where k_{top} indexes the K' highest $s^{(k)}$.

3. **Parameter Update:**

$$\Theta \leftarrow \Theta - \eta \nabla_{\Theta} (\mathcal{L}_{\text{guide}} + \lambda \|\hat{\mathbf{Y}}_{t+1} - \tilde{\mathbf{Y}}_{t+1}\|_2^2) \quad (13)$$

The frozen VQ-VAE acts as an uncertainty-aware teacher: $\mathcal{L}_{\text{guide}}$ aligns predictions with metric-optimal reconstructions. Ensemble distillation $\tilde{\mathbf{Y}}_{t+1}$ mitigates exposure bias through data augmentation. Hyperparameter λ balances direct supervision and distributional smoothing

2.4. Inference Stage with Beam Search

We propose a novel beam search protocol that synergizes the base predictor f_{Θ} with the diversity-generating VQ-VAE

h_Φ . The algorithm maintains B candidate trajectories to balance exploration (via codebook variations) and exploitation (through metric-guided selection), crucial for chaotic systems where small deviations amplify exponentially. The procedure (Algorithm 1) operates in three phases:

Initialization: Generate K initial variants from \mathbf{X}_t using the VQ-VAE’s decoding diversity

Iterative Rollout: At each step n , expand B candidates into $B \times K$ possibilities using the codebook

Trajectory Selection: Retain top- B paths based on accumulated scores $s_n^{(b,k)} = \sum_{m=t+1}^n S(\tilde{\mathbf{Y}}_m^{(b,k)})$

Algorithm 1: Beam Search with Codebook Variations

Input: Initial state $\mathbf{X}_t \in \mathbb{R}^{C \times H \times W}$, beam width B , horizon N

Output: Optimal trajectory $\{\tilde{\mathbf{Y}}_{t+1}^*, \dots, \tilde{\mathbf{Y}}_{t+N}^*\}$

// Phase 1: Initialization

$\hat{\mathbf{Y}}_{t+1} \leftarrow f_\Theta(\mathbf{X}_t)$

$\{\tilde{\mathbf{Y}}_{t+1}^{(k)}\}_{k=1}^K \leftarrow h_\Phi(\hat{\mathbf{Y}}_{t+1})$

$\mathcal{B}_{t+1} \leftarrow \text{Top-}B \left(\{(\tilde{\mathbf{Y}}_{t+1}^{(k)}, S(\tilde{\mathbf{Y}}_{t+1}^{(k)}))\}_{k=1}^K \right)$

// Phase 2: Iterative Rollout

for $n \leftarrow t + 2$ **to** $t + N$ **do**

$\mathcal{C}_n \leftarrow \emptyset$

foreach beam $b \in \mathcal{B}_{n-1}$ **do**

$\hat{\mathbf{Y}}_n^{(b)} \leftarrow f_\Theta(\tilde{\mathbf{Y}}_{n-1}^{(b)})$

$\{\tilde{\mathbf{Y}}_n^{(b,k)}\}_{k=1}^K \leftarrow h_\Phi(\hat{\mathbf{Y}}_n^{(b)})$

for $k \leftarrow 1$ **to** K **do**

$s_n^{(b,k)} \leftarrow s_{n-1}^{(b)} + \alpha^{n-t} S(\tilde{\mathbf{Y}}_n^{(b,k)})$

$\mathcal{C}_n \leftarrow \mathcal{C}_n \cup \{(\{\tilde{\mathbf{Y}} \text{ sequence}\}, s_n^{(b,k)})\}$

end

end

$\mathcal{B}_n \leftarrow \arg \max_{\substack{\mathcal{S} \subset \mathcal{C}_n \\ |\mathcal{S}|=B}} \sum_{(\cdot, s) \in \mathcal{S}} s$

end

// Phase 3: Terminal Selection

$\{\tilde{\mathbf{Y}}^*\} \leftarrow \arg \max_{(\mathcal{Y}, s) \in \mathcal{B}_{t+N}} s$

return $\{\tilde{\mathbf{Y}}_{t+1}^*, \dots, \tilde{\mathbf{Y}}_{t+N}^*\}$

Key Enhancements Our beam search extends conventional approaches through:

- **Codebook-Driven Diversity:** The VQ-VAE generates K physically-plausible variations at each step, avoiding mode collapse in chaotic systems. For weather prediction, this captures alternative storm trajectories that single-point estimates miss.
- **Exponential Score Discounting (Wang et al., 2024):**

The term α^{n-t} ($\alpha \in (0, 1]$) in the scoring function prioritizes recent accuracy, crucial for non-stationary processes. This implements:

$$s_n^{(b,k)} = \sum_{m=t+1}^n \alpha^{n-m} S(\tilde{\mathbf{Y}}_m^{(b,k)}) \quad (14)$$

- **Dynamic Beam Pruning:** The selection operator $\arg \max_{\mathcal{S}}$ solves a knapsack-like optimization to maximize total score while maintaining beam width B . This is equivalent to:

$$\mathcal{B}_n = \underset{(\cdot, s) \in \mathcal{S}}{\text{maximize}} \sum s \quad \text{s.t. } |\mathcal{S}| \leq B \quad (15)$$

The whole algorithm of the proposed BeamVQ is summarized in Algorithm 2.

Algorithm 2: Unified Framework of BeamVQ

Input: Historical observations \mathbf{X}_t , prediction horizon N

Output: Optimal trajectory $\{\tilde{\mathbf{Y}}_{t+1}^*, \dots, \tilde{\mathbf{Y}}_{t+N}^*\}$

// Stage 1: Base Model Training

Initialize predictor f_Θ

Train f_Θ via $\min_{\Theta} \|\hat{\mathbf{Y}}_{t+1} - \mathbf{Y}_{t+1}\|_2^2$

// Stage 2: VQ-VAE Codebook Learning

Learn encoder e_Φ , decoder d_Φ , codebook \mathcal{C}

Generate K variants $\{\tilde{\mathbf{Y}}_{t+1}^{(k)}\}$ per prediction

// Stage 3: Joint Optimization

while not converged **do**

 Generate candidates $\{\tilde{\mathbf{Y}}_{t+1}^{(k)}\}$ via h_Φ

 Select best candidate $\tilde{\mathbf{Y}}_{t+1}^*$ using metric M

 Update f_Θ with $\tilde{\mathbf{Y}}_{t+1}^*$ and top- K' ensemble

end

// Stage 4: Beam Search Inference

Initialize beam with top- B candidates

for $n = t + 1$ **to** $t + N$ **do**

 Expand each beam with K codebook variants

 Keep top- B trajectories by accumulated scores

end

return Best trajectory from final beam

3. Experiment

In this section, we verify the effectiveness of our method by evaluating 5 benchmarks and 10 backbone models. The experiments aim to answer the following research questions: **RQ1.** Can BeamVQ enhance the performance of the baselines? **RQ2.** How does BeamVQ perform under data-scarce conditions? **RQ3.** Can BeamVQ have better physical alignment? **RQ4.** Can BeamVQ produce long-term forecasting? Appendix D also has additional results.

Table 1: Performance comparison of various models with and without the BeamVQ method across five benchmark tests (SWE(u), RBC, NSE, Prometheus, SEVIR), using MSE as the evaluation metric. We bold-case the entries with lower MSE. ‘‘Improvement’’ represents the average percentage improvement in MSE achieved with BeamVQ.

MODEL	BENCHMARKS									
	SWE (u)		RBC		NSE		PROMETHEUS		SEVIR	
	ORI	+ BEAMVQ	ORI	+ BEAMVQ	ORI	+ BEAMVQ	ORI	+ BEAMVQ	ORI	+ BEAMVQ
RESNET	0.0076	0.0033	0.1599	0.1283	0.2330	0.1663	0.2356	0.1987	0.0671	0.0542
CONVLSTM	0.0024	0.0016	0.2726	0.0868	0.4094	0.1277	0.0732	0.0533	0.1757	0.1283
EARTHFORMER	0.0135	0.0093	0.1273	0.1093	1.8720	0.1202	0.2765	0.2001	0.0982	0.0521
SIMVP-v2	0.0013	0.0010	0.1234	0.1087	0.1238	0.1022	0.1238	0.0921	0.0063	0.0032
TAU	0.0046	0.0031	0.1221	0.0965	0.1205	0.1017	0.1201	0.0899	0.0059	0.0029
EARTHFASEER	0.0075	0.0059	0.1454	0.1023	0.1138	0.0987	0.1176	0.1092	0.0065	0.0021
FNO	0.0031	0.0024	0.1235	0.1053	0.2237	0.1005	0.3472	0.2275	0.0783	0.0436
NMO	0.0021	0.0004	0.1123	0.1092	0.1007	0.0886	0.0982	0.0475	0.0045	0.0029
CNO	0.0146	0.0016	0.1327	0.1086	0.2188	0.1483	0.1097	0.0254	0.0056	0.0053
FOURCASTNET	0.0065	0.0061	0.0671	0.0219	0.1794	0.1424	0.0987	0.0542	0.0721	0.0652
IMPROVEMENT(%)	+39.08%		+18.97%		+35.83%		+33.65%		+35.27%	

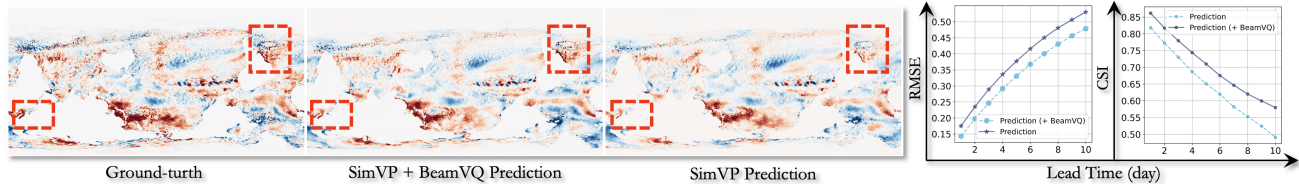


Figure 3: The prediction results of marine extreme heatwave events include: A visual comparison (from left to right): ground truth labels, SimVP+BeamVQ prediction results on day 10, and SimVP prediction results on day 10. The cumulative changes of RMSE over prediction time. The cumulative changes of CSI over prediction time.

3.1. Experimental Settings

Benchmarks & Backbones. Our dataset spans multiple spatiotemporal dynamical systems, summarized as follows: • **Real-world Datasets**, including SEVIR (Veillette et al., 2020); • **Equation-driven Datasets**, focusing on PDE (Takamoto et al., 2022) (Navier-Stokes equations, Shallow-Water Equations) and Rayleigh-Bénard convection flow (Wang et al., 2020); (3) **Computational Fluid Dynamics Simulation Datasets**, namely Prometheus (Wu et al., 2024b). We select core models from three different fields for analysis. Specifically: • **Spatio-temporal Predictive Learning**, we choose ResNet (He et al., 2016), ConvLSTM (Shi et al., 2015), Earthformer (Gao et al., 2022), SimVP-v2 (Tan et al., 2022), TAU (Tan et al., 2023), Earthfarseer (Wu et al., 2024a), and FourcastNet (Pathak et al., 2022) as representative models; • **Neural Operator**, we compare models like FNO (Li et al., 2020), NMO (Wu et al., 2024c) and CNO (Raonic et al., 2023);

Metric. We use Mean Squared Error (MSE) as the evaluation metric to assess each model’s prediction performance. Additionally, to thoroughly evaluate the model’s performance on specific tasks, we employ metrics such as Root Mean Squared Error (RMSE), Critical Success Index (CSI), Structural Similarity Index (SSIM), relative L2 error, and

Turbulent Kinetic Energy (TKE). More details can be found in Appendix A.

Implementation details. Our method trains with MSE loss, uses the ADAM optimizer (Kingma & Ba, 2014), and sets the learning rate to 10^{-3} . We set the batch size to 10. The training process early stops within 500 epochs. Additionally, we set our code bank size as 1024×64 , beam size K as 5 or 10, and the threshold as the first quartile of all candidate’s scores, which we find suitable for all backbones. We implement all experiments in PyTorch (Paszke et al., 2019). Training and inference for all our experiments run on a single NVIDIA A100-PCIE-40GB GPU.

Table 2: Comparison of backbones on marine heatwaves to evaluate BeamVQ’s ability to capture extreme events.

MODEL	MSE		PROMOTION (%)
	ORI	+BEAMVQ	
U-NET	0.0968	0.0848	12.40%
CONVLSTM	0.1204	0.0802	33.38%
SIMVP	0.0924	0.0653	29.33%

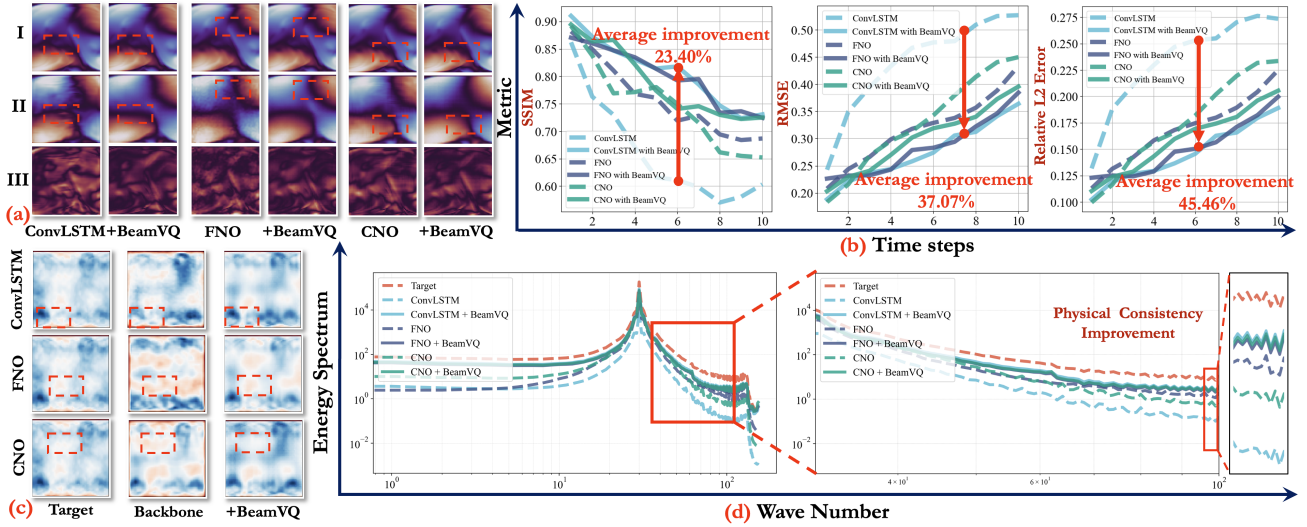


Figure 4: **The BeamVQ plugin improves physical consistency and prediction accuracy.** (a) shows a visual comparison of the actual target, predicted results, and errors at different time steps. (b) displays the changes in SSIM, RMSE, and relative L2 error over time steps. (c) compares the turbulent TKE. (d) presents the energy spectrum at different wavenumbers.

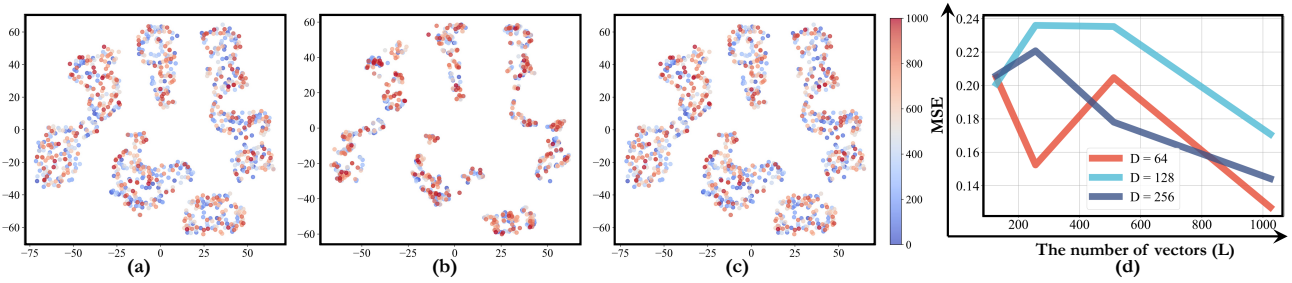


Figure 5: The t-SNE visualization in (a), (b), and (c) shows the Ground-truth, ConvLSTM and ConvLSTM+BeamVQ predictions, respectively. (d) shows the analysis of the Codebank parameters.

3.2. BeamVQ improves all backbone models (RQ1)

As shown in Table 1, BeamVQ significantly improves performance across five benchmark tests and ten backbone models. After introducing BeamVQ, all models show a decreasing trend in MSE, with average improvements ranging from 18.97% to 39.08%. For example, in the RBC fluid convection task, ConvLSTM’s MSE decreases from 0.2726 to 0.0868 (a 68.15% improvement), indicating a strong enhancement in capturing complex physical dynamics. Earthformer’s MSE in the NSE turbulence prediction task drops sharply from 1.8720 to 0.1202 (a 93.58% improvement), demonstrating BeamVQ’s advantage in modeling high-dimensional chaotic systems. Even advanced models like SimVP-v2 and TAU see MSE reductions of 49.21% and 50.85%, respectively, in the SEVIR extreme weather prediction task, proving BeamVQ’s compatibility with advanced architectures. In the Prometheus combustion dynamics task, the FNO operator reduces MSE by 34.47% (from 0.3472 to 0.2275), highlighting its enhanced ability

to incorporate physical constraints. FourcastNet’s MSE in the RBC task decreases from 0.0671 to 0.0219 (a 67.36% improvement). The lightweight ResNet model’s MSE in the SWE shallow water equations task drops by 56.58% (from 0.0076 to 0.0033), demonstrating that significant accuracy gains can be achieved without complex architectures.

3.3. BeamVQ helps alleviate data scarcity (RQ2)

In scientific computing, data scarcity is a core challenge. We use extreme marine heatwaves as a scenario closely linked to human activities and economic development. To evaluate model performance, we adopt RMSE (numerical accuracy) and CSI (extreme-event capture). We compare U-Net, ConvLSTM, and SimVP as backbone networks. Table 2 and Figure 3 present the results, followed by our analysis. First, Table 2 shows that BeamVQ significantly lowers MSE on the extreme marine heatwave task (e.g., ConvLSTM’s error decreases from 0.1204 to 0.0802, SimVP’s from 0.0924 to 0.0653). Even in data-scarce scenarios, these models

better capture dynamic changes and improve overall prediction accuracy. Second, Figure 3 compares day-10 visualizations and plots RMSE and CSI over time, indicating that BeamVQ generates distributions closer to the real sea temperature fields. The cumulative RMSE remains lower for models with BeamVQ, and CSI stays high, suggesting stronger sensitivity to extreme events and more accurate forecasts throughout the prediction period.

3.4. BeamVQ Boosts Physical Alignment (RQ3)

Figure 4 shows that BeamVQ significantly enhances physical consistency and prediction accuracy. In Figure 4(a), comparing actual targets, predicted results, and errors at different time steps reveals better detail and physical consistency with smaller errors when using BeamVQ. Figure 4(b) shows that BeamVQ improves SSIM by 23.40%, and reduces RMSE and relative L2 error by 37.07% and 45.46%, respectively, indicating stronger robustness in spatiotemporal prediction. Figure 4(c) compares turbulent kinetic energy (TKE), demonstrating more accurate capture of TKE changes, especially in small-scale turbulence. Figure 4(d) displays the energy spectrum at different wavenumbers, where BeamVQ maintains better physical consistency in high-wavenumber regions—indicative of more accurate small-scale vortex prediction. Overall, BeamVQ not only improves numerical accuracy but also better captures the essence of physical phenomena.

3.5. BeamVQ Excels In Long-term Dynamic System Forecasting (RQ4)

In our long-term forecasting experiments on the SWE benchmark, we compare different backbone models by evaluating the relative L2 error for three variables (U, V, and H). We input 5 frames and predict 50 frames. For the SimVP-v2 model, using BeamVQ reduces the relative L2 error for SWE (u) from 0.0187 to 0.0154, SWE (v) from 0.0387 to 0.0342, and SWE (h) from 0.0443 to 0.0397, with the 3D visualization of SWE (h) shown in Figure 6 [I]. For ConvLSTM, applying BeamVQ reduces the relative L2 error for SWE (u) from 0.0487 to 0.0321, SWE (v) from 0.0673 to 0.0351, and SWE (h) from 0.0762 to 0.0432. For FNO, using BeamVQ reduces the relative L2 error for SWE (u) from 0.0571 to 0.0502, SWE (v) from 0.0832 to 0.0653, and SWE (h) from 0.0981 to 0.0911. These results, obtained under a consistent experimental protocol, underscore the efficacy of BeamVQ in systematically mitigating prediction errors over extended time horizons, thereby enhancing the stability and robustness of each model’s forecasts. Overall, BeamVQ significantly enhances the long-term forecasting accuracy of these backbone models, offering promising implications for its application in complex dynamical systems and real-world fluid dynamics scenarios.

Table 3: We compare different backbones on the SWE Benchmark for Long-term Forecasting.

MODEL		SWE		
		(U)	(V)	(H)
SIMVP-V2	ORI	0.0187	0.0387	0.0443
	+BEAMVQ	0.0154	0.0342	0.0397
CONVLSTM	ORI	0.0487	0.0673	0.0762
	+BEAMVQ	0.0321	0.0351	0.0432
FNO	ORI	0.0571	0.0832	0.0981
	+BEAMVQ	0.0502	0.0653	0.0911
CNO	ORI	0.1283	0.1422	0.1987
	+BEAMVQ	0.0621	0.0674	0.0965

Table 4: Ablation studies on the NSE benchmark.

VARIANTS	MSE	TKE
FNO	0.2237	0.3964
FNO+BEAMVQ	0.1005	0.1572
FNO+BEAMVQ (w/o BEAMS)	0.1207	0.2003
FNO+BEAMVQ (w/o SELFT)	0.1118	0.1872
FNO+BEAMVQ (w. MSE)	0.1654	0.2847
FNO+VQVAE	0.1872	0.3652
FNO+PINO	0.1249	0.2342

3.6. Interpretation Analysis & Ablation Study

Qualitative Analysis Using t-SNE. Figure 5 shows t-SNE visualizations on the RBC dataset: (a) ground truth, (b) ConvLSTM predictions, and (c) ConvLSTM + BeamVQ predictions. In (a), the ground truth has clear clusters. In (b), ConvLSTM’s clustering is blurry with overlaps, indicating limited capability in capturing data structure. In (c), ConvLSTM + BeamVQ yields clearer clusters closer to the ground truth, demonstrating that BeamVQ significantly enhances the model’s predictive accuracy and physical consistency.

Analysis on Code Bank. We train FNO+BeamVQ on NSE for 100 epochs with a learning rate of 0.001 and batch size of 100. In the VQVAE codebank dimension experiment, increasing the number of vectors L notably reduces MSE. When $L = 1024$ and $D = 64$, the MSE reaches a minimum of 0.1271. Although MSE fluctuates more at $L = 256$ or 512, overall, higher L helps improve accuracy. Most training losses quickly stabilize within 20 epochs; $L = 512$ and $D = 128$ notably shows higher stability, but $L = 1024$ and $D = 64$ achieves the lowest MSE.

Ablation Study. We use NSE with FNO for ablation. Variants: (I) FNO; (II) FNO+BeamVQ; (III) FNO+BeamVQ (w/o Beamsearch); (IV) FNO+BeamVQ (w/o self-Training); (V) FNO+BeamVQ (w MSE); (VI) FNO+VQVAE; (VII) FNO+PINO (Li et al., 2024). Table 4 shows FNO starts

with an MSE of 0.2237 and a TKE error of 0.3964. Adding BeamVQ drops them to 0.1005 and 0.1572. Omitting Beam-search or self-training increases MSE but still outperforms the base. VQVAE and PINO yield MSEs of 0.1872 and 0.1249, with TKE errors of 0.3652 and 0.2342. Overall, BeamVQ significantly enhances accuracy.

4. Conclusion

We propose BeamVQ, a unified framework for spatio-temporal forecasting in data-scarce settings. By combining VQ-VAE with beam search, BeamVQ addresses limited labeled data, captures extreme events, and maintains physical consistency. It first learns main dynamics via a deterministic base model, then encodes predictions with Top-K VQ-VAE to produce diverse, plausible outputs. A joint optimization process guided by domain-specific metrics boosts accuracy and extreme event sensitivity. During inference, beam search retains multiple candidate trajectories, balancing exploration of rare phenomena with likely system trajectories. Extensive experiments on weather and fluid dynamics tasks show improved prediction accuracy, robust extreme state detection, and strong physical consistency. Ablation studies confirm the crucial roles of vector quantization and beam search in enhancing performance.

Acknowledgements

This work was supported by the National Natural Science Foundation of China (42125503, 42430602).

References

Anonymous. Open-CK: The non-linear chaotic combustion kinetics benchmark, 2024. URL <https://openreview.net/forum?id=mKFFEXeIQS>.

Bi, K., Xie, L., Zhang, H., Chen, X., Gu, X., and Tian, Q. Accurate medium-range global weather forecasting with 3d neural networks. *Nature*, 619(7970):533–538, 2023.

Caruana, R., Niculescu-Mizil, A., Crew, G., and Ksikes, A. Ensemble selection from libraries of models. In *Proceedings of the twenty-first international conference on Machine learning*, pp. 18, 2004.

Cranmer, M., Greydanus, S., Hoyer, S., Battaglia, P., Spergel, D., and Ho, S. Lagrangian neural networks. *arXiv preprint arXiv:2003.04630*, 2020.

Dosovitskiy, A. An image is worth 16x16 words: Transformers for image recognition at scale. *arXiv preprint arXiv:2010.11929*, 2020.

Doswell III, C. A. Severe convective storms—an overview. *Severe convective storms*, pp. 1–26, 2001.

Du, J., Grave, E., Gunel, B., Chaudhary, V., Celebi, O., Auli, M., Stoyanov, V., and Conneau, A. Self-training improves pre-training for natural language understanding. *arXiv preprint arXiv:2010.02194*, 2020.

Frölicher, T. L., Fischer, E. M., and Gruber, N. Marine heatwaves under global warming. *Nature*, 560(7718): 360–364, 2018.

Gao, Z., Shi, X., Wang, H., Zhu, Y., Wang, Y. B., Li, M., and Yeung, D.-Y. Earthformer: Exploring space-time transformers for earth system forecasting. *Advances in Neural Information Processing Systems*, 35:25390–25403, 2022.

Gao, Z., Shi, X., Han, B., Wang, H., Jin, X., Maddix, D., Zhu, Y., Li, M., and Wang, Y. B. Prediff: Precipitation nowcasting with latent diffusion models. *Advances in Neural Information Processing Systems*, 36, 2023.

Greydanus, S., Dzamba, M., and Yosinski, J. Hamiltonian neural networks. *Advances in neural information processing systems*, 32, 2019.

Griebel, M., Dornseifer, T., and Neunhoffer, T. *Numerical simulation in fluid dynamics: a practical introduction*. SIAM, 1998.

Guen, V. L. and Thome, N. Disentangling physical dynamics from unknown factors for unsupervised video prediction. In *Proceedings of the IEEE/CVF conference on computer vision and pattern recognition*, pp. 11474–11484, 2020.

Han, M., Feng, S., Chen, C. P., Xu, M., and Qiu, T. Structured manifold broad learning system: A manifold perspective for large-scale chaotic time series analysis and prediction. *IEEE Transactions on Knowledge and Data Engineering*, 31(9):1809–1821, 2018.

Hansen, D., Maddix, D. C., Alizadeh, S., Gupta, G., and Mahoney, M. W. Learning physical models that can respect conservation laws. In *International Conference on Machine Learning*, pp. 12469–12510. PMLR, 2023.

He, K., Zhang, X., Ren, S., and Sun, J. Deep residual learning for image recognition. In *Proceedings of the IEEE conference on computer vision and pattern recognition*, pp. 770–778, 2016.

Jouvet, G., Huss, M., Blatter, H., Picasso, M., and Rappaz, J. Numerical simulation of rhonegletscher from 1874 to 2100. *Journal of Computational Physics*, 228(17): 6426–6439, 2009.

Karlbauer, M., Cresswell-Clay, N., Durran, D. R., Moreno, R. A., Kurth, T., Bonev, B., Brenowitz, N., and Butz, M. V. Advancing parsimonious deep learning weather prediction using the healpix mesh. *Journal of Advances in Modeling Earth Systems*, 16(8):e2023MS004021, 2024.

- Karnopp, D. C., Margolis, D. L., and Rosenberg, R. C. *System dynamics: modeling, simulation, and control of mechatronic systems*. John Wiley & Sons, 2012.
- Karpatne, A., Atluri, G., Faghmous, J. H., Steinbach, M., Banerjee, A., Ganguly, A., Shekhar, S., Samatova, N., and Kumar, V. Theory-guided data science: A new paradigm for scientific discovery from data. *IEEE Transactions on knowledge and data engineering*, 29(10):2318–2331, 2017.
- Kingma, D. P. and Ba, J. Adam: A method for stochastic optimization. *arXiv preprint arXiv:1412.6980*, 2014.
- Krishnapriyan, A., Gholami, A., Zhe, S., Kirby, R., and Mahoney, M. W. Characterizing possible failure modes in physics-informed neural networks. *Advances in Neural Information Processing Systems*, 34:26548–26560, 2021.
- Kumar, T., Brennan, R., Mileo, A., and Bendechache, M. Image data augmentation approaches: A comprehensive survey and future directions. *IEEE Access*, 2024.
- Lam, R., Sanchez-Gonzalez, A., Willson, M., Wyrnsberger, P., Fortunato, M., Alet, F., Ravuri, S., Ewalds, T., Eaton-Rosen, Z., Hu, W., et al. Graphcast: Learning skillful medium-range global weather forecasting. *arXiv preprint arXiv:2212.12794*, 2022.
- Leutbecher, M. and Palmer, T. Ensemble forecasting. *Journal of Computational Physics*, 227(7):3515–3539, 2008. ISSN 0021-9991. doi: <https://doi.org/10.1016/j.jcp.2007.02.014>. URL <https://www.sciencedirect.com/science/article/pii/S0021999107000812>. Predicting weather, climate and extreme events.
- Li, Z., Kovachki, N., Azizzadenesheli, K., Liu, B., Bhattacharya, K., Stuart, A., and Anandkumar, A. Fourier neural operator for parametric partial differential equations. *arXiv preprint arXiv:2010.08895*, 2020.
- Li, Z., Zheng, H., Kovachki, N., Jin, D., Chen, H., Liu, B., Azizzadenesheli, K., and Anandkumar, A. Physics-informed neural operator for learning partial differential equations. *ACM/JMS Journal of Data Science*, 2021.
- Li, Z., Zheng, H., Kovachki, N., Jin, D., Chen, H., Liu, B., Azizzadenesheli, K., and Anandkumar, A. Physics-informed neural operator for learning partial differential equations. *ACM / IMS J. Data Sci.*, feb 2024. doi: 10.1145/3648506. URL <https://doi.org/10.1145/3648506>. Just Accepted.
- Long, Z., Lu, Y., Ma, X., and Dong, B. PDE-net: Learning PDEs from data. In *International conference on machine learning*, pp. 3208–3216. PMLR, 2018.
- Lorenz, E. Predictability: Does the flap of a butterfly’s wing in brazil set off a tornado in texas? 1972.
- Moisy, F. and Jiménez, J. Geometry and clustering of intense structures in isotropic turbulence. *Journal of fluid mechanics*, 513:111–133, 2004.
- Oliver, E. C., Donat, M. G., Burrows, M. T., Moore, P. J., Smale, D. A., Alexander, L. V., Benthuisen, J. A., Feng, M., Sen Gupta, A., Hobday, A. J., et al. Longer and more frequent marine heatwaves over the past century. *Nature communications*, 9(1):1–12, 2018.
- Orszag, S. A. and Israeli, M. Numerical simulation of viscous incompressible flows. *Annual Review of Fluid Mechanics*, 6(1):281–318, 1974.
- Paszke, A., Gross, S., Massa, F., Lerer, A., Bradbury, J., Chanan, G., Killeen, T., Lin, Z., Gimelshein, N., Antiga, L., et al. Pytorch: An imperative style, high-performance deep learning library. *Advances in neural information processing systems*, 32, 2019.
- Pathak, J., Subramanian, S., Harrington, P., Raja, S., Chattopadhyay, A., Mardani, M., Kurth, T., Hall, D., Li, Z., Azizzadenesheli, K., et al. Fourcastnet: A global data-driven high-resolution weather model using adaptive fourier neural operators. *arXiv preprint arXiv:2202.11214*, 2022.
- Pukrushpan, J. T., Stefanopoulou, A. G., and Peng, H. *Control of fuel cell power systems: principles, modeling, analysis and feedback design*. Springer Science & Business Media, 2004.
- Raissi, M., Perdikaris, P., and Karniadakis, G. E. Physics-informed neural networks: A deep learning framework for solving forward and inverse problems involving nonlinear partial differential equations. *Journal of Computational physics*, 378:686–707, 2019.
- Raonic, B., Molinaro, R., De Ryck, T., Rohner, T., Bartolucci, F., Alaifari, R., Mishra, S., and de Bézenac, E. Convolutional neural operators for robust and accurate learning of pdes. *Advances in Neural Information Processing Systems*, 36, 2023.
- Ravuri, S., Lenc, K., Willson, M., Kangin, D., Lam, R., Mirowski, P., Fitzsimons, M., Athanassiadou, M., Kashem, S., Madge, S., et al. Skillful precipitation nowcasting using deep generative models of radar. *Nature*, 597(7878):672–677, 2021.
- Rogallo, R. S. and Moin, P. Numerical simulation of turbulent flows. *Annual review of fluid mechanics*, 16(1): 99–137, 1984.

- Shi, X., Chen, Z., Wang, H., Yeung, D.-Y., Wong, W.-K., and Woo, W.-c. Convolutional lstm network: A machine learning approach for precipitation nowcasting. *Advances in neural information processing systems*, 28, 2015.
- Steinbiss, V., Tran, B.-H., and Ney, H. Improvements in beam search. In *ICSLP*, volume 94, pp. 2143–2146, 1994.
- Sun, L., Gao, H., Pan, S., and Wang, J.-X. Surrogate modeling for fluid flows based on physics-constrained deep learning without simulation data. *Computer Methods in Applied Mechanics and Engineering*, 361:112732, 2020.
- Takamoto, M., Praditia, T., Leiteritz, R., MacKinlay, D., Alesiani, F., Pflüger, D., and Niepert, M. Pdebench: An extensive benchmark for scientific machine learning. *Advances in Neural Information Processing Systems*, 35: 1596–1611, 2022.
- Tan, C., Gao, Z., Li, S., and Li, S. Z. Simvp: Towards simple yet powerful spatiotemporal predictive learning. *arXiv preprint arXiv:2211.12509*, 2022.
- Tan, C., Gao, Z., Wu, L., Xu, Y., Xia, J., Li, S., and Li, S. Z. Temporal attention unit: Towards efficient spatiotemporal predictive learning. In *Proceedings of the IEEE/CVF Conference on Computer Vision and Pattern Recognition*, pp. 18770–18782, 2023.
- Tramèr, F., Kurakin, A., Papernot, N., Goodfellow, I., Boneh, D., and McDaniel, P. Ensemble adversarial training: Attacks and defenses. *arXiv preprint arXiv:1705.07204*, 2017.
- Veillette, M., Samsi, S., and Mattioli, C. Sevir: A storm event imagery dataset for deep learning applications in radar and satellite meteorology. *Advances in Neural Information Processing Systems*, 33:22009–22019, 2020.
- Wang, C., Li, S., He, D., and Wang, L. Is l2 physics informed loss always suitable for training physics informed neural network? *Advances in Neural Information Processing Systems*, 35:8278–8290, 2022a.
- Wang, H. and Wang, Y. Self-ensemble adversarial training for improved robustness. *arXiv preprint arXiv:2203.09678*, 2022.
- Wang, K., Wu, H., Duan, Y., Zhang, G., Wang, K., Peng, X., Zheng, Y., Liang, Y., and Wang, Y. Nuwadynamics: Discovering and updating in causal spatio-temporal modeling. In *The Twelfth International Conference on Learning Representations*, 2024.
- Wang, R., Kashinath, K., Mustafa, M., Albert, A., and Yu, R. Towards physics-informed deep learning for turbulent flow prediction. In *Proceedings of the 26th ACM SIGKDD international conference on knowledge discovery & data mining*, pp. 1457–1466, 2020.
- Wang, Y., Jiang, L., Yang, M.-H., Li, L.-J., Long, M., and Fei-Fei, L. Eidetic 3d lstm: A model for video prediction and beyond. In *International conference on learning representations*, 2018.
- Wang, Y., Wu, H., Zhang, J., Gao, Z., Wang, J., Philip, S. Y., and Long, M. Predrnn: A recurrent neural network for spatiotemporal predictive learning. *IEEE Transactions on Pattern Analysis and Machine Intelligence*, 45(2):2208–2225, 2022b.
- Wu, H., Wang, C., Xu, F., Xue, J., Chen, C., Hua, X.-S., and Luo, X. Pure: Prompt evolution with graph ode for out-of-distribution fluid dynamics modeling. In *The Thirty-eighth Annual Conference on Neural Information Processing Systems*.
- Wu, H., Xion, W., Xu, F., Luo, X., Chen, C., Hua, X.-S., and Wang, H. Pastnet: Introducing physical inductive biases for spatio-temporal video prediction. *arXiv preprint arXiv:2305.11421*, 2023.
- Wu, H., Liang, Y., Xiong, W., Zhou, Z., Huang, W., Wang, S., and Wang, K. Earthfarsser: Versatile spatio-temporal dynamical systems modeling in one model. In *Proceedings of the AAAI Conference on Artificial Intelligence*, volume 38, pp. 15906–15914, 2024a.
- Wu, H., Wang, H., Wang, K., Wang, W., Ye, C., Tao, Y., Chen, C., Hua, X.-S., and Luo, X. Prometheus: Out-of-distribution fluid dynamics modeling with disentangled graph ode. In *Proceedings of the 41st International Conference on Machine Learning*, pp. PMLR 235, Vienna, Austria, 2024b. PMLR.
- Wu, H., Zhou, S., Huang, X., and Xiong, W. Neural manifold operators for learning the evolution of physical dynamics, 2024c. URL <https://openreview.net/forum?id=SQnOmOzqAM>.
- Zhang, H. mixup: Beyond empirical risk minimization. *arXiv preprint arXiv:1710.09412*, 2017.
- Zhang, Y., Long, M., Chen, K., Xing, L., Jin, R., Jordan, M. I., and Wang, J. Skilful nowcasting of extreme precipitation with nowcastnet. *Nature*, 619(7970):526–532, 2023.
- Zhu, Y., Zabarar, N., Koutsourelakis, P.-S., and Perdikaris, P. Physics-constrained deep learning for high-dimensional surrogate modeling and uncertainty quantification without labeled data. *Journal of Computational Physics*, 394: 56–81, 2019.

A. Metric

Mean Squared Error (MSE) Mean Squared Error (MSE) is a common statistical metric used to assess the difference between predicted and actual values. The formula is:

$$MSE = \frac{1}{n} \sum_{i=1}^n (y_i - \hat{y}_i)^2 \quad (16)$$

where n is the number of samples, y_i is the actual value, and \hat{y}_i is the predicted value.

Relative L2 Error Relative L2 error measures the relative difference between predicted and actual values, commonly used in time series prediction. The formula is:

$$\text{Relative L2 Error} = \frac{\|Y_{\text{pred}} - Y_{\text{true}}\|_2}{\|Y_{\text{true}}\|_2} \quad (17)$$

where Y_{pred} is the predicted value and Y_{true} is the actual value.

Structural Similarity Index Measure (SSIM) The Structural Similarity Index (SSIM) measures the similarity between two images in terms of luminance, contrast, and structure. The formula is:

$$SSIM(x, y) = \frac{(2\mu_x\mu_y + C_1)(2\sigma_{xy} + C_2)}{(\mu_x^2 + \mu_y^2 + C_1)(\sigma_x^2 + \sigma_y^2 + C_2)} \quad (18)$$

where μ_x and μ_y are the mean values, σ_x and σ_y are the standard deviations, σ_{xy} is the covariance.

B. Related Work

- **Numerical Methods and Ensemble Forecasting:** they are the traditional methods to realize physical spatial-temporal forecasting (Jouvet et al., 2009; Rogallo & Moin, 1984; Orszag & Israeli, 1974; Griebel et al., 1998), which employ discrete approximation techniques to solve sets of equations derived from physical laws. Although these physics-driven methods ensure compliance with fundamental principles such as conservation laws (Karpatne et al., 2017; Karnopp et al., 2012; Pukrushpan et al., 2004), they require highly trained professionals for development (Lam et al., 2022), incur high computational costs (Pathak et al., 2022), are less effective when the underlying physics is not fully known (Takamoto et al., 2022), and cannot easily improve as more observational data become available (Lam et al., 2022). Moreover, traditional numerical methods usually perturb initial observation inputs with different random noises, which can alleviate the problem of observation errors. Then Ensemble Forecasting (Leutbecher & Palmer, 2008; Karlbauer et al., 2024) can average the outputs of different noisy inputs to improve the robustness.
- **Data-Driven Methods:** Recently, data-driven deep learning starts to revolutionize the space of space-time forecasting for complex physical systems (Gao et al., 2022; Wu et al., 2024a; Li et al., 2020; Tan et al., 2022; Shi et al., 2015; Pathak et al., 2022; Wu et al., 2023; Bi et al., 2023; Lam et al., 2022; Zhang et al., 2023). Rather than relying on differential equations governed by physical laws, the data-driven approach constructs model by optimizing statistical metrics such as Mean Squared Error (MSE), using large-scale datasets. These methods (Wang et al., 2022b; Shi et al., 2015; Wang et al., 2018; Tan et al., 2022; Gao et al., 2022; Wu et al., 2024a) are orders of magnitude faster, and excel in capturing the intricate patterns and distributions present in high-dimensional nonlinear systems (Pathak et al., 2022). Despite their success, purely data-driven methods fall short in generating physically plausible predictions, leading to unreliable outputs that violate critical constraints (Bi et al., 2023; Pathak et al., 2022; Wu et al., 2024c).

Previous works have tried to combine physics-driven methods and data-driven methods to get the best of both worlds. Some methods try to embed physical constraints in the neural network (Long et al., 2018; Greydanus et al., 2019; Cranmer et al., 2020; Guen & Thome, 2020). For example, PhyDNet (Guen & Thome, 2020) adds a physics-inspired PhyCell in the recurrent network. However, such methods require explicit formulation of the physical rules along with specialized designs for network architectures or training algorithms. As a result, they lack flexibility and cannot easily adapt to different backbone architectures. Another type of methods (Raissi et al., 2019; Li et al., 2021; Hansen et al., 2023), best exemplified by the Physics-Informed Neural Network (PINN) (Raissi et al., 2019), leverages physical equations as additional regularizers in neural network training (Hansen et al., 2023). Physics-Informed Neural Operator (PINO) (Li et al., 2021) extends the data-driven Fourier Neural Operator (FNO) to be physics-informed by adding

soft regularizers in the loss function. However, PDE-based regularizers not only impose multiple-object optimization challenges (Krishnapriyan et al., 2021; Wang et al., 2022a) but also only work in limited scenarios where has simplified physical equations and fixed boundary conditions. More recently, PreDiff (Gao et al., 2023) trains a latent diffusion model for probabilistic forecasting, and guides the model’s sampling process with a physics-informed energy function. However, PreDiff requires training a separate knowledge alignment network to integrate the physical constraints, which is not needed in our method.

Most importantly, all the above-mentioned works require large-scale datasets to train for good performance, while collecting scientific data can be expensive and even infeasible sometimes. Still worse, they can suffer from the poor prediction of extreme events, since there are sparse and imbalance extreme event data even in the large datasets.

- **Data Augmentation:** CV has a long history of employing data augmentation to improve generalization. Traditionally, almost all CV works manipulate the semantic invariance in images to conduct various data pre-processing, such as random cropping, resizing, flipping, rotation, color normalization, and so on (Kumar et al., 2024). More recently, CV has developed advanced techniques, such as mixup, to generate new data samples by combining different images and their labels, which can achieve even better generalization. However, these data augmentation techniques are domain-specific, which is based on the domain knowledge of CV (Kumar et al., 2024). Other fields, such as NLP, audio, and physical spatiotemporal forecasting, cannot directly adopt the same data augmentation techniques.
- **Self-training:** it has proved to be an effective semi-supervised learning method that exploits the extra unlabeled data (Du et al., 2020). Typically, self training first gives the pseudo labels on the unable data. Then it estimates the confidence of its own classification, and adds the high-confidence samples into training sets to improve the model training. However, our work does not have access to extra unlabeled data, making it improper to employ the existing self-training strategies.
- **Self-ensemble:** it is well known that Ensemble methods can enhance the performance (Caruana et al., 2004) and improve the robustness (Tramèr et al., 2017). Since Ensemble of different models needs high training costs of multiple models, self-ensemble (Wang & Wang, 2022) typically makes use of different states in the training process to be free of extra training costs. However, existing self-ensemble cannot explore rare but critical phenomena beyond the original dataset.

C. Detailed Mathematical Proof

Proof of Theorem 1

Now we have N augmented data and we need to select the best from them. We consider both the quality and the diversity of these data and get the sampling strategy from an optimization problem.

We model the sampling strategy as a multinomial distribution supported on all the augmented data $S = \{\mathbf{X}_j\}_{j=1}^N$, which means that the sampling strategy $\pi = (\pi_1, \dots, \pi_N)^\top$ is the corresponding probabilities of selecting $\mathbf{X}_1, \dots, \mathbf{X}_N$, then we can model the expectation of the similarity as:

$$\begin{aligned} & \mathbb{E}_{Y_x, Y_{x'} \in \mathcal{C}} \{g(x, x') \mid S\} \\ &= \int g(\mathbf{x}, \mathbf{x}') \pi(\mathbf{x}) \Pr_S(Y_x \in \mathcal{C} \mid \mathbf{x} = \mathbf{x}) \pi(\mathbf{x}') \Pr_S(Y_{x'} \in \mathcal{C} \mid \mathbf{x} = \mathbf{x}') dx dx' \\ &= \sum_{i,j=1}^N g(\mathbf{X}_i, \mathbf{X}_j) \pi_i \pi_j \Pr_S(Y_x \in \mathcal{C} \mid \mathbf{x} = \mathbf{X}_i) \Pr_S(Y_{x'} \in \mathcal{C} \mid \mathbf{x} = \mathbf{X}_j), \end{aligned}$$

where the set \mathcal{C} denotes the criterion of selection we are using, the function g can be chosen as any similarity metric function and x means a random variable.

The core to solving the above optimization problem is to use predictive inference to approximate the conditional probability of $\{Y_x \in \mathcal{C}\}$ given $x = \mathbf{X}$. Let $\mu(\mathbf{x}) := \mathbb{E}(Y \mid \mathbf{X} = \mathbf{x})$ be the oracle associated with (\mathbf{X}, Y) . Denote $\theta_j = \mathbb{I}\{Y_j \in \mathcal{C}\}$. As the augmented data $\mathbf{X}_1, \dots, \mathbf{X}_N$ are independently identically distributed, $\theta_1, \dots, \theta_N$ can be regarded as independent Bernoulli(q) variables with $q = \Pr(Y_j \in \mathcal{C})$. The probability distribution of the predicted result W_j for $j = 1, \dots, N$ is

$$\Pr(W_j \mid \theta_j) = (1 - \theta_j) f_0 + \theta_j f_1,$$

where f_0 and f_1 are the conditional distributions of W_j on $Y_j \in \mathcal{C}$ or not.

Denote $T(w) = \frac{(1-g)f_0(W_j)}{f(W_j)}$, we can rewrite the expectation of the similarity as

$$\mathbb{E}_{Y_x, Y_{x'} \in \mathcal{C}} \{g(x, x') | S\} = \sum_{i,j=1}^N g(\mathbf{X}_i, \mathbf{X}_j) \pi_i \pi_j (1 - T_i)(1 - T_j) = \boldsymbol{\pi}^\top A_{\mathbb{T}} \boldsymbol{\pi},$$

Next, we use the expectation to control the quality of the data.

$$\mathbb{E}\{\mathbb{I}(Y_x \notin \mathcal{C}) | S\} = \sum_{i=1}^N \Pr(Y_i \notin \mathcal{C} | \mathbf{X}_i) \pi_i = \sum_{i=1}^N \pi_i T_i \leq \alpha,$$

In all, the optimization problem can be modeled as

$$\arg \min_{\boldsymbol{\pi}} h(\boldsymbol{\pi}, \mathbb{T}) := \boldsymbol{\pi}^\top A_{\mathbb{T}} \boldsymbol{\pi}, \tag{19}$$

$$\text{subject to } \begin{cases} \sum_{i=1}^N \pi_i T_i \leq \alpha, \\ \sum_{i=1}^N \pi_i = 1, \\ 0 \leq \pi_i \leq m^{-1}, \quad 1 \leq i \leq N. \end{cases} \tag{20}$$

where m is used to control the maximum selection.

The best selection of K is determined by the strategy $\boldsymbol{\pi}$ which serves as the solution to the above optimization problem.

D. Additional Experiments

D.1. Long-term forecasting experiment expansion

In the long-term forecasting experiments, we compare the performance of different backbone models on the SWE benchmark, evaluating the relative L2 error for three variables (U, V, and H). Our setup inputs 5 frames and predicts 50 frames. For the SimVP-v2 model, using BeamVQ reduces the relative L2 error for SWE (u) from 0.0187 to 0.0154, SWE (v) from 0.0387 to 0.0342, and SWE (h) from 0.0443 to 0.0397. We visualize SWE (h) in 3D as shown in Figure 6 [I]. For the ConvLSTM model, applying BeamVQ reduces the relative L2 error for SWE (u) from 0.0487 to 0.0321, SWE (v) from 0.0673 to 0.0351, and SWE (h) from 0.0762 to 0.0432. For the FNO model, using BeamVQ reduces the relative L2 error for SWE (u) from 0.0571 to 0.0502, SWE (v) from 0.0832 to 0.0653, and SWE (h) from 0.0981 to 0.0911. Overall, BeamVQ significantly improves the long-term forecasting accuracy of different backbone models.

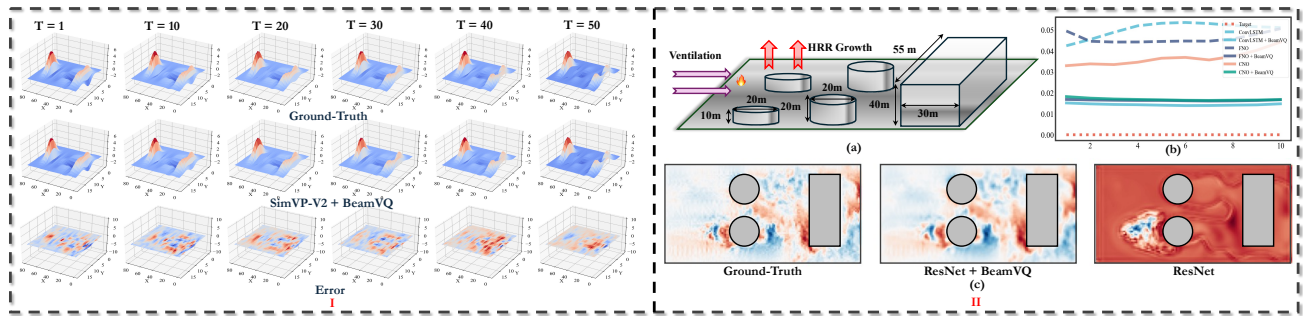


Figure 6: **I.** 3D visualization of the SWE(h), showing Ground-truth, SimVP-V2+BeamVQ predictions, and Error at T=1, 10, 20, 30, 40, 50. **II.** A case study. Building fire simulation with ventilation settings added to Wu’s Prometheus (Wu et al., 2024b). (a) Layout and HRR growth. (b) Comparison of physical metrics for different methods. (c) Ground-truth, ResNet+BeamVQ, and ResNet predictions.

D.2. Experiment Statistical Significance

To measure the statistical significance of our main experiment results, we choose three backbones to train on two datasets to run 5 times. Table 5 records the average and standard deviation of the test MSE loss. The results prove that our method is statistically significant to outperform the baselines because our confidence interval is always upper than the confidence interval of the baselines. Due to limited computation resources, we do not cover all ten backbones and five datasets, but we believe these results have shown that our method has consistent advantages.

Table 5: The average and standard deviation of MSE in 5 runs

MODEL	BENCHMARKS			
	NSE		SEVIR	
	ORI	+ BEAMVQ	ORI	+ BEAMVQ
CONVLSTM	0.4092±0.0002	0.1277±0.0001	0.1762 0.0007	0.1279±0.0009
FNO	0.2227±0.0003	0.1007 ±0.0002	0.0787±0.0012	0.0437±0.0013
CNO	0.2192 ±0.0008	0.1492±0.0011	0.0057±0.0005	0.0053±0.0006